JWST Peers into the Class I Protostar TMC1A: Atomic Jet and Spatially Resolved Dissociative Shock Region

The Astrophysical Journal Letters, 951:L32 (7pp), 2023 July 10 https://doi.org/10.3847/2041-8213/acdfca

JWST Peers into the Class I Protostar TMC1A: Atomic Jet and Spatially Resolved Dissociative Shock Region

D. Harsono[1], P. Bjerkeli[2], J. P. Ramsey[3], K. M. Pontoppidan[4], L. E. Kristensen[5], J. K. Jørgensen[5], H. Calcutt[6], Z-Y. Li[3], and A. Plunkett[7]
[1] Institute of Astronomy, Department of Physics, National Tsing Hua University, Hsinchu, Taiwan; dharsono@gapp.nthu.edu.tw
[2] Chalmers University of Technology, Department of Space, Earth and Environment, SE-412 96 Gothenburg, Sweden
[3] Department of Astronomy, University of Virginia, Charlottesville, VA 22904, USA
[4] Space Telescope Science Institute, 3700 San Martin Drive, Baltimore, MD 21218, USA
[5] Niels Bohr Institute, University of Copenhagen, Øster Voldgade 5–7, DK-1350 Copenhagen K., Denmark
[6] Institute of Astronomy, Faculty of Physics, Astronomy and Informatics, Nicolaus Copernicus University in Toruń, ul. Grudzikadzka 5, 87–100 Toruń, Poland
[7] National Radio Astronomy Observatory, 520 Edgemont Road, Charlottesville, VA 22903, USA
Received 2023 February 13; revised 2023 May 31; accepted 2023 June 12; published 2023 July 10

Abstract

Outflows and winds launched from young stars play a crucial role in the evolution of protostars and the early stages of planet formation. However, the specific details of the mechanism behind these phenomena, including how they affect the protoplanetary disk structure, are still debated. We present JWST NIRSpec integral field unit observations of atomic and H_2 lines from 1 to 5.1 μm toward the low-mass protostar TMC1A. For the first time, a collimated atomic jet is detected from TMC1A in the [Fe II] line at 1.644 μm along with corresponding extended H_2 2.12 μm emission. Toward the protostar, we detected spectrally broad H I and He I emissions with velocities up to 300 km s^{-1} that can be explained by a combination of protostellar accretion and a wide-angle wind. The 2 μm continuum dust emission, H I, He I, and O I all show emission from the illuminated outflow cavity wall and scattered line emission. These observations demonstrate the potential of JWST to characterize and reveal new information about the hot inner regions of nearby protostars; in this case, a previously undetected atomic wind and ionized jet in a well-known outflow.

Unified Astronomy Thesaurus concepts: Jets (870); H I line emission (690); Young stellar objects (1834); Protostars (1302)

Supporting material: data behind figure

1. Introduction

The formation and growth of a protostellar system require material to collapse and accrete onto a central mass via gravity, and these effects are observable as infalling motion (e.g., Leung & Brown 1977; Snell & Loren 1977) and accretion (e.g., Herbig 1977; Hartmann & Kenyon 1985). However, the most visually prominent manifestation of ongoing star formation is bipolar outflows that can be traced through atomic (e.g., Mundt & Fried 1983; Persson et al. 1984) and molecular (e.g., Bally & Lada 1983; Snell et al. 1990; Davis et al. 2002) gas lines. Outflows are an important part of any protostellar system since they remove angular momentum from the protoplanetary disk that orbits the forming protostar. This further aids the accretion process from the disk toward the protostar (e.g., Frank et al. 2014). The removal of material by the outflow may also affect the physical structure of the disk, and therefore potentially influence the disk evolution, with consequences for any planets that eventually form in the disk (e.g., Pascucci et al. 2022).

Protostellar outflows are often described as consisting of a collimated jet and a slower wide-angle wind, even though distinctions between the components and their physical origins are debated (Arce et al. 2007). The jet component denotes the fast and collimated outflow that is likely responsible for entrainment on scales >5000 au as observed through, e.g., CO emission (Rabenanahary et al. 2020; de A. Schutzer et al. 2022). Meanwhile, a slower wide-angle disk wind points to the small-scale (<500 au) outflow which is closely related to the protoplanetary disk. Observationally, both jet and wide-angle wind components should be detectable in the IR and submillimeter. Protostellar jets are observed through high-velocity $\gtrsim$100 km s^{-1} rotational transitions of ^{12}CO and SiO in the submillimeter (e.g., Tafalla et al. 2004; Hirano et al. 2010; Plunkett et al. 2015; Hull et al. 2016; Ray & Ferreira 2021) in addition to shocked gas tracers in the infrared such as [O I] 63 μm, [Fe II] 1.64 μm, and H_2 2.12 μm lines (e.g., Hartigan et al. 1994; Nisini et al. 2004; Gusdorf et al. 2017; Yang et al. 2022). The slower disk wind is typically seen using rotational transitions of ^{12}CO and SO in the submillimeter (Podio et al. 2015; Bjerkeli et al. 2016; Tabone et al. 2017; de Valon et al. 2020) along with O I lines in the IR (Pascucci et al. 2022).

The Class I protostar TMC1A (IRAS 04365+2535) is an embedded ~0.45 $M_\odot$ (Harsono et al. 2018) protostar in the Taurus Molecular cloud (140 pc; Galli et al. 2019). It has a large-scale bipolar ^{12}CO molecular outflow that extends to at least 6000 au (Yıldız et al. 2015). Atacama Large Millimeter/submillimeter Array (ALMA) observations of the $J = 2 - 1$ rotational transition of ^{12}CO at 1.3 mm (Bjerkeli et al. 2016) show a molecular disk wind emanating from the protoplanetary disk. Fast-moving gas is also seen in ground-based, high-spectral-resolution (~3 km s^{-1}) observations of rovibrational lines of ^{12}CO (4.6 μm) that show hot (>1000 K) molecular gas moving at radial velocities of ~75 km s^{-1} (~93 km s^{-1} when accounting for an inclination of $i = 54°$; Harsono et al. 2021),

indicative of a disk wind (Herczeg et al. 2011). Despite the detections of the slow disk-wind component, a jet component of TMC1A has not previously been detected in SiO (Harsono et al. 2021) or water lines (Kristensen et al. 2012).

JWST provides the spectral ($R = 2700$) and spatial resolution (0.″1) needed to understand better the nature of the outflow around TMC1A. With the Near Infrared Spectrograph (NIRSpec; Jakobsen et al. 2022) instrument, the hot ($T_{\rm gas} > 1000$ K) atomic and molecular gas has been mapped in the vicinity of TMC1A at wavelengths between 0.9 and 5 μm. In this letter, we present the first detection of a jet through [Fe II] emission. We also report and analyze the hot atomic and molecular lines from H I, He I, O I, [Fe II], and H_2 coming from the inner regions of the protostar. In combination with archival data from other observatories, these results provide the means to start building a comprehensive picture of the TMC1A protostellar+outflow system.

2. JWST Observations and Calibration

JWST observed TMC1A on 2022 September 2 using the NIRSpec integral field unit (IFU) mode (PID: 2104; PI: Harsono; doi:10.17909/6k3w-1948). JWST NIRSpec provides high-spectral-resolution data from ∼0.97 to 5.28 μm, nominally across a 30×30 grid of 0.″1 "spaxels" (14 au at 140 pc). The F100LP (1–1.9 μm), F170LP (1.7–3.2 μm), and F290LP (2.9–5.3 μm) filters were used with the G140H, G235H, and G395H dispersers for the highest spectral resolution ($R \sim 2700$ or $\Delta v = 90$–150 km s^{-1}; Jakobsen et al. 2022). The exposure times were 15,719 s, 4123 s, and 2577 s for the F100LP, F170LP, and F290LP filters, respectively. Target acquisition was performed with Wide Aperture Target Acquisition using the full subarray in the F110W filter, and data were obtained using the NRSRAPID readout pattern with an exposure time of 42.9 s. The science observations were taken with a medium CYCLING dither pattern and a total of six dithers for each filter. The science integration was taken with 4, 15, and 60 groups in the F100LP, F170LP, and F290LP filters, respectively. For this letter, we concentrate on the gas lines in the wavelength range between 0.97 and ∼2 μm where we detect many atomic lines, and we will present the complete data in a follow-up work.

We reprocessed the Stage 2 products as processed through the JWST pipeline, version 1.9.6 (Bushouse et al. 2023) with the calibration files CRDS JWST_1088.PMAP (Greenfield & Miller 2016). To produce IFU spectral cubes, additional rejections were applied to remove outliers in the stage 2 products before passing them through the stage 3 step of the pipeline. A flux-calibrated spectrum has been extracted from the central square aperture of 0.″3 centered on the brightest spaxel. The systematic variation in the velocity resolution is approximately 50–100 km s^{-1} (1–2 channels).

We used the National Institute of Standards and Technology (NIST) atomic spectra database (Kramida 2010) and the atomic line list of van Hoof (2018) to obtain the properties of transitions for H, He, O, and Fe. A local average of the dust continuum emission is subtracted from each emission line before creating zeroth moment maps. The statistical noise of each map is calculated from emission-free regions (spatially and spectrally). In addition to the JWST observations, we include archival ALMA observations (Harsono et al. 2021; PID: 2017.1.00212.S) and Hubble Space Telescope (HST) observations with the Near Infrared Camera and Multi-Object Spectrometer (NICMOS) in the F160W filter (PID: 7325; PI: Terebey; doi:10.17909/6k3w-1948). These data are used to align the images (see Appendix A) and to compare the emission morphology at different wavelengths.

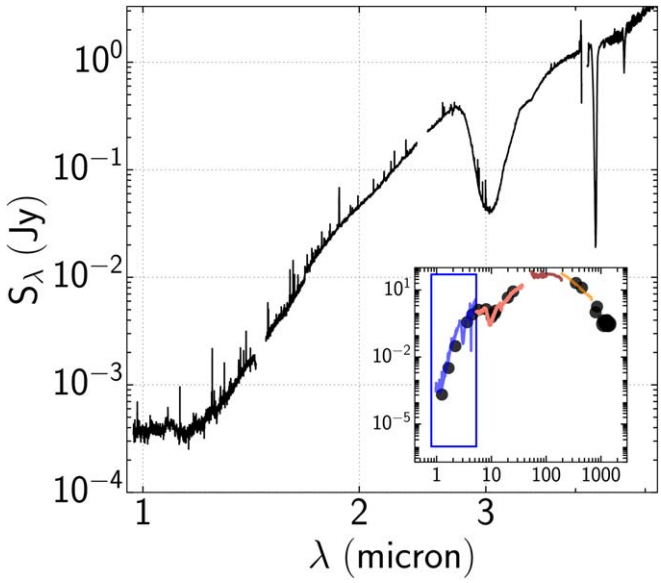

Figure 1. NIRSpec spectrum extracted from the central 0.″3 spaxels. The spectral energy distribution of TMC1A from other observations is shown in the inset along with the NIRSpec data in blue. The photometric data points (black) are from Kristensen et al. (2012; which include points from Skrutskie et al. 2006; Di Francesco et al. 2008; Evans et al. 2009; Karska et al. 2013; Green et al. 2013). The Herschel PACS observations of Green et al. (2013) are shown in orange. The SPITZER IRS spectrum (pink; Lahuis et al. 2010) is overlaid. The extracted NIRSpec spectrum is available as data-behind-the-figure.

(The data used to create this figure are available.)

3. Results

The observed near-infrared (NIR) spectrum from 1 to 5 μm toward TMC1A is shown in Figure 1. The flux density spans >4 orders of magnitude between a few microjansky at ∼1 μm and ∼0.2 Jy at ∼2.8 μm. The complete spectral energy distribution is also shown in the inset of Figure 1 to indicate where our spectrally resolved observations fit in. The photometric data are retrieved from Kristensen et al. (2012) and the spectrum from the Spitzer "Cores to Disks" (c2d) program (Lahuis et al. 2010). Flux densities in the 70–200 μm range are taken from the Herschel "Dust, Ice, and Gas in Time" (DIGIT) program (Green et al. 2013). By including JWST data, TMC1A now has continuous spectral coverage at moderately high spectral resolution from ∼1 μm up to ∼200 μm. In this paper, we only analyze the spectrally resolved data toward the brightest spaxel.

Figure 2 shows the normalized spectrum with lines from H I, He I, O I, and Fe II indicated. The spectrum was normalized using piece-wise polynomials of degrees 5–7 fitted to the line-free channels. Numerous gas lines are detected down to ∼1% of the continuum but we concentrate on the brightest atomic and molecular lines only for this study.

Figure 2 (bottom) shows the spectrally resolved H I Paschen series ($n_{\rm final} = 3$) and Brackett series ($n_{\rm final} = 4$) lines, which are detected at high signal-to-noise ratios (>10 based on the statistical noise around each line). The H I lines in the Paschen series show an asymmetric, redshifted line profile with peaks of

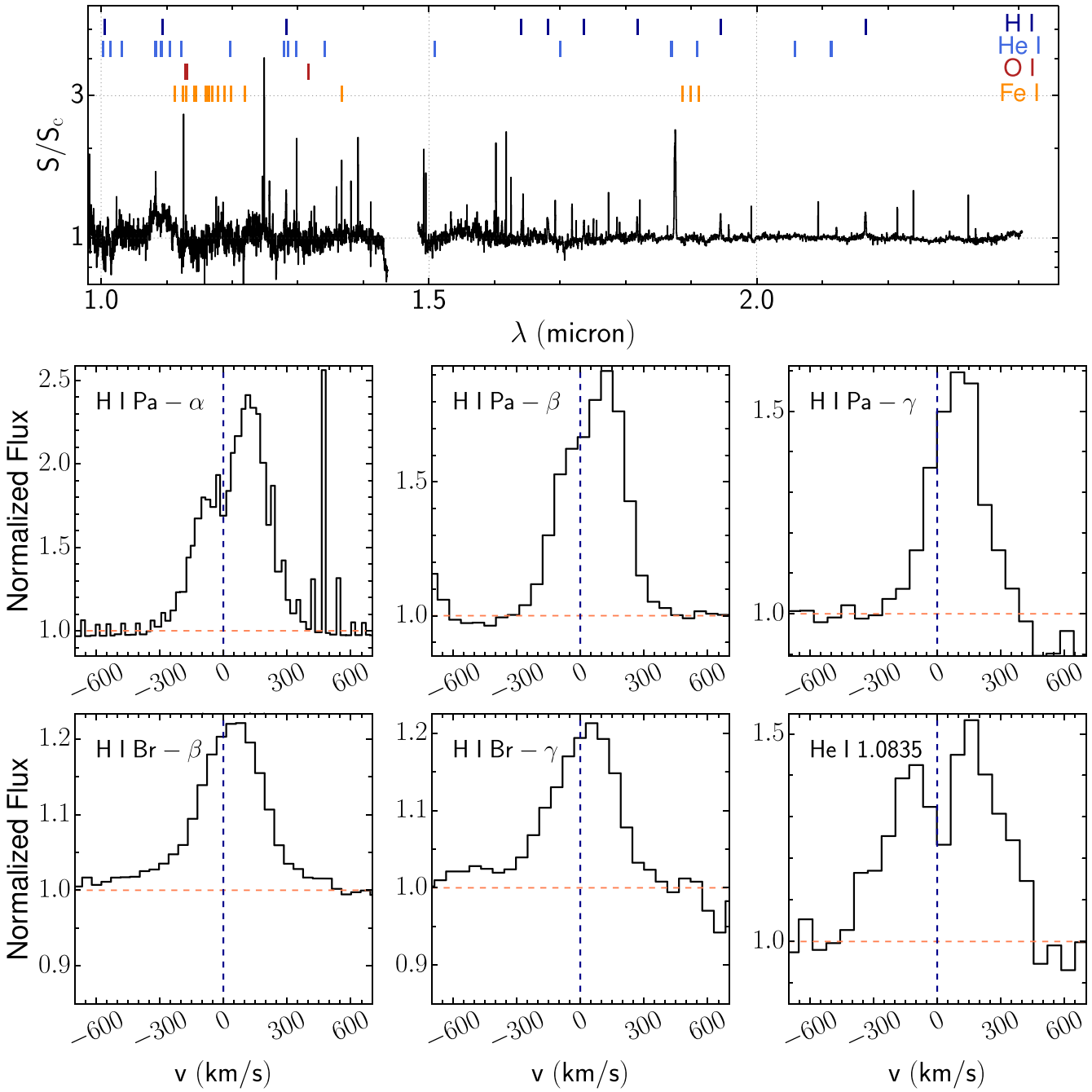

Figure 2. Top: normalized spectrum of TMC1A. The spectrum has been normalized with a global continuum fit constructed with polynomials of degrees 5 to 7. Transitions of H I, He I, O I, and Fe II with high A_{ij} values are indicated by the vertical colored lines above the spectrum. Bottom: zoom-in spectra of the brightest H I lines and the He I λ10835 line. The spectral resolution is $\Delta v \sim 100$–150 km s^{-1}.

the different lines located at $v \sim 100$ km s^{-1}. The broad, red asymmetric line profile could be indicative of wind emission, similar to previously detected rovibrational fundamental mode ($v = 1 - 0$) lines of CO (see Appendix B; Herczeg et al. 2011). The Brackett lines are similarly broad, but less asymmetric, where the profiles with the peak intensity of the lines shifting to a slower velocity of ∼50 km s^{-1}.

H I lines are thought primarily to trace the magnetospheric accretion flows and/or partially ionized disk winds (Edwards et al. 2006; Erkal et al. 2022). By integrating the H I lines between −400 and 400 km s^{-1}, we find equivalent widths (EWs) of the Paα and Paβ lines between 300 and 550 km s^{-1} (∼10–35 Å). The measured line strengths are similar to previous H I studies of the outflows from classical T Tauri disks (Muzerolle et al. 1998a; Edwards et al. 2013). Paschen and Brackett line ratios can be used to estimate the density and temperature of the gas. We find that the integrated line ratios for TMC1A are Paα/Pa$\beta \simeq 1.8$, Paβ/Pa$\gamma \simeq 1.6$, and Brγ/Pa$\beta \simeq 0.27$. Using the models of Kwan & Fischer (2011), these line ratios indicate emission from hot dense gas with $n_{\rm H} > 10^9$ cm^{-3} and $T_{\rm gas} > 5000$ K.

Assuming that the line emission is dominated by magnetospheric accretion, the H I line luminosity can be used to infer the stellar accretion. Since the measured EW is similar to those of classical T Tauri disks, we follow Muzerolle et al. (1998a) to estimate the accretion rate of TMC1A. The measured integrated

$EW_{Pa\beta} = 305$ km s^{-1} translates to $L_{Pa\beta} = 7.17 \times 10^{-8}\,L_\odot$. Using the $L_{Pa\beta}$–L_{acc} relation, we obtain $\dot{M} \sim 2 \times 10^{-12}\,M_\odot$ yr^{-1}, which is much lower than expected for a Class I source. Meanwhile, the Brγ line (2.1661 μm) has an EW ~ 73 km s^{-1}, which translates to an accretion rate of $\dot{M} \sim 3 \times 10^{-9}\,M_\odot$ yr^{-1}. Note that both line ratios and accretion rates are calculated without accounting for any extinction.

Based on the bolometric luminosity (2.7 $L_\odot$; Kristensen et al. 2012) and the protostellar mass (0.45 $M_\odot$; Harsono et al. 2021), the expected accretion rate is $\sim 1 \times 10^{-6}\,M_\odot$ yr^{-1}. A rate of $\sim 5.6 \times 10^{-6}\,M_\odot$ yr^{-1} can be estimated using the envelope density model of Furlan et al. (2008). Through the comparison of these two accretion rates, the upper limit to the visual extinction is $A_v = 10 - 30$ ($A_J = 0.3\,A_V$; Pontoppidan et al. 2004). Meanwhile, the measured H I Paβ/Paγ and Brγ/Paβ ratios suggests $A_V < 5$ as compared to Edwards et al. (2013). With the spatial information afforded by the NIRSpec IFU, it is possible to constrain how the extinction toward TMC1A varies with position, but this is left to a future study.

We also detect and spectrally resolved the He I 1S-1Po λ10835 line (Figure 2). The line is double peaked with a similar line width as the H I Paα line. This He I line can also be used to trace magnetospheric accretion and the disk wind (Edwards et al. 2006; Erkal et al. 2022). The deficit of blueshifted absorption may indicate that the line emission originates from the dense jet and disk wind with a minor contribution from magnetospheric accretion. Meanwhile, the O I and [Fe II] lines are narrow with typical line widths of 1–2 channels.

The zeroth moment maps of the atomic and H_2 2.12 μm lines can be used to highlight the physical components of TMC1A on 50 au scales, which are shown in Figure 3. In order to orient the data with respect to the disk and ^{12}CO wind, we overlay the HST and ALMA 230 GHz dust continuum data on top of the JWST 2 μm continuum map in panel (a). The second panel (b) shows the extended H I Paα line with a similar structure as the 2 μm dust continuum. Note that the cold molecular wind ($T_{gas} \sim 60$ K) that is traced by the ^{12}CO $J = 2 - 1$ line with ALMA is inside of the H I emission. Panels (c) and (d) respectively show the He I and O I zeroth moment maps overlaid on top of the [Fe II] emission map. Blue and red contours continue to mark the submillimeter ^{12}CO wind. The [Fe II] emission is extended while both the He and O line emissions concentrate around the dust continuum peak. Finally, the [Fe II] and the $v = 1$–0 S(1)H_2 integrated maps are shown in panel (e), where they show a similar extended structure. The peak of the [Fe II] emission is slightly offset from H_2.

4. Discussion

Our JWST NIRSPEC observations show spectrally resolved atomic and molecular lines between 1 and 5 μm. We detected broad atomic emission lines (>200 km s^{-1}) from the central 0.″3 region. With the IFU, we also see linearly extended emission in the direction of the outflow traced by [Fe II] and H_2. Finally, we detect diffuse atomic emission on source that overlaps with the NIR continuum emission. We will discuss the origin of each observable features below and the implications for protostellar accretion and outflows.

In contrast to the more evolved Class II disks, the broad H I and He I line profiles observed toward TMC1A indicate a significant contribution from the jet and wind in addition to magnetospheric accretion (Nisini et al. 2004; Edwards et al. 2006). Magnetospheric accretion models tend to produce narrow ($\Delta v \sim 100$ km s^{-1}) line profiles with inverse P Cygni absorption (Muzerolle et al. 1998b; Kurosawa et al. 2006). Given how broad our line profiles are, it is likely that the outflow (jet, entrained gas, and the wind) is the dominant source of emission at the brightest spaxel as presented in this letter. In accretion or disk-wind scenarios, the observed emission comes from the largely neutral gas that is either collisionally excited or from recombination lines. The observed Paβ/Paγ line ratio is similar to that of the luminous Class I protostar HH100 IRS (>1.4; Nisini et al. 2004), which is consistent with a partially ionized gas. To estimate the physical conditions of the gas from the observed line ratios, we use the Kwan & Fischer (2011) model that includes the local excitation of H I. The line ratio indicates optically thick ($\tau \sim 10$) H I emission with a column density between 10^{10} and 10^{12} cm^{-2}. If the gas temperature is closer to 5000 K, a higher density of H I is needed to explain the observed line ratio. Toward TMC1A, the rovibrational $v = 2$–1 line of ^{12}CO also exhibits a broad profile ($\Delta v \sim 96$ km s^{-1}) similar to HH100 IRS with temperatures of $\sim$1000 K (Herczeg et al. 2011). If both lines probe a similar region within the central 0.″1–0.″2 (14–28 au), the data are tracing the high-density gas with temperatures >1000 K caused by both accretion and outflow.

The extended [Fe II] and H_2 emissions correspond to the jet that drives the large-scale CO outflow. Emission from [Fe II] tends to trace dissociative shocks along the jet (Allen & Burton 1993) with velocities $\gtrsim$40 km s^{-1} (May et al. 2000) at densities of $\sim 10^4$ cm^{-3} (McCoey et al. 2004). [Fe II] is expected to emit from internal shocks of the jet where faster material catches up and shocks against slower-moving material that has been ejected earlier. Meanwhile, H_2 emission is expected to trace the slower shock component behind the knots. Figure 3 shows that the H_2 emission peaks are offset by 30–40 au from [Fe II]. It is usually suggested that extended H_2 shocked gas traces the wide-angle wind that surrounds the jet (Davis et al. 2002; Agra-Amboage et al. 2014) that is responsible for opening the outflow cavity. Toward TMC1A, H_2 emission is concentrated in a small conical region around the Fe jet while the H I emission is more extended as their emission is scattered by dust grains. H_2 emission seems clumpy near the upper layers of the disk that is caused by either extinction or the physical conditions surrounding the jet-launching region. In general, H_2 emission can be explained by either H_2 reformation in the wake of the leading bow shock of a jet or the presence of H_2 in the shell around the [Fe II] jet.

The origins of protostellar outflows are still debated, and two physically related launching mechanisms have emerged as the primary explanations: a wide-angle magnetohydrodynamic (MHD) wind (e.g., Mundt & Fried 1983; Pudritz & Norman 1983) and an X-wind model (e.g., Shu et al. 1994; Shang et al. 2007). The wide-angle wind (disk wind) is launched from the protoplanetary disk's surface while an X-wind is launched from a narrow region where the inner, dust-free disk's ($T_{dust} > 1400$ K) magnetic field and the protostar's magnetosphere interact. In future analyses, we will combine multiple atomic and H_2 lines to assess whether or not the protostellar outflow from TMC1A is consistent with the proposed launching mechanisms.

The outflow cavity wall is traced by the dust continuum emission as seen in HST and JWST 2 μm images. These structures are visible due to light scattering by micron-sized grains along the cavity wall. The arc that is highlighted by the

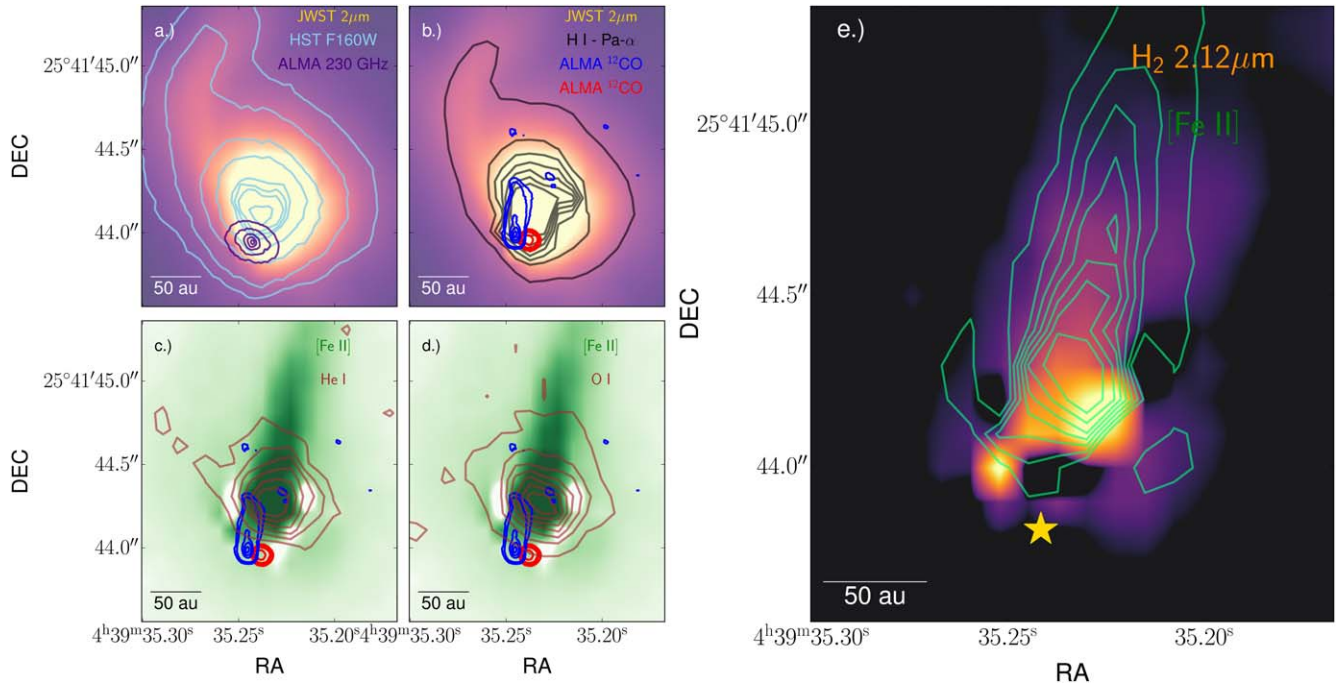

Figure 3. (a.) JWST 2 μm continuum map is shown in color. A linear scale between 0.5% and 99% of the intensity distribution is used. We have overlaid the HST F160W and ALMA 230 GHz continuum maps on top of the 2 μm map to orient our results with respect to previous observations. The contours are chosen to highlight the features of the HST image and the location of the millimeter dust disk. (b.) The integrated H I Paα map is shown by the black contour lines on top of the 2 μm map. Contours from 95% to 98% of the intensity distribution are used. ALMA observations of the blue- and redshifted rotational transition of ^{12}CO ($J = 2 - 1$) are shown by the blue and red contours, respectively. The ^{12}CO $J = 2 - 1$ line is only showing velocities >1.5 km s^{-1} from systemic. The contours are chosen to highlight the orientation of the ^{12}CO $J = 2 - 1$ gas. (c.) A comparison between [Fe II] 1.644 μm, He I λ10835, and ^{12}CO $J = 2 - 1$ line emission. The integrated [Fe II] line is shown in the background in green with a linear scale spanning between 60% and 99% of the intensity distribution. The He I map is shown by the brown contours with levels from 95% to 97% of the intensity distribution. (d.) A comparison between the [Fe II] 1.644 μm, O I λ1.12, and ^{12}CO $J = 2 - 1$ lines. The contours of O I (in brown) are also showing the brightest components (95%–97% of the intensity distribution). (e.) The integrated [Fe II] map is overlaid on top of the integrated H_2 2.12 μm map. The H_2 map is drawn with colors spanning from 5σ up to the peak intensity. The green contours show [Fe II] but only the brightest pixels in the map (>96% of the intensity distribution). The center of the millimeter dust disk is indicated by the star. In each panel, a 50 au scale bar is show in the bottom left.

2 μm continuum and H I line emission could be due to local overdensities of micron-sized dust grains as a result of interactions with the wind and protostellar radiation, potentially even an illuminated accretion stream, or scattered line emission. The opening angle of the outflow cavity as traced by the dust emission appears larger than the extent of the H_2 emission. The presence of H I along the arc could be tracing the dissociation of H_2 along the cavity wall by UV photons or shocks near the cavity produced by a disk wind or X-wind. In the X-wind picture, the dissociation comes from the shocked gas as the wind interacts with the infalling envelope (e.g., Shang et al. 2007, 2020). With the slower disk wind, additional UV radiation from the protostar is needed to dissociate the molecular material along the cavity wall (Kristensen et al. 2013). The main criticism against fast, steady X-winds is that they would disrupt the protostellar envelope within ~1000 yr given the observed protostellar envelope structures around low-mass stars (Liang et al. 2020). From the outflow of TMC1A and the disk-to-stellar mass ratio (Harsono et al. 2021), the protostellar age of TMC1A is $>10^4$ yr. Alternatively, the extended H I emission is tracing unresolved emission from magnetospheric accretion and/or the wind as the line emission is forward scattered by dust grains along the arc. Therefore, the H I line emission is as extended as the dust arc. These observations are therefore more consistent with an extended disk-wind model carving out the outflow cavity that is directly illuminated by feedback (radiation and mechanical) from the accretion and outflow.

JWST is shedding light on the anatomy of the inner hot regions around TMC1A. Combined with constraints from ALMA data, in Figure 4, we present a cartoon of the different physical components as traced by the different emission lines shown. The components are a planet-forming disk, accretion, jet/wind, and outflow cavity wall. With NIRspec, we now have access to high-spatial resolution observations of atomic and molecular tracers that can trace accretion and ejection directly along with their associated feedback on the immediate surroundings, which are crucial information for improving our understanding of how stars form.

Acknowledgments

This work is based on observations made with the NASA/ESA/CSA James Webb Space Telescope. The data were obtained from the Mikulski Archive for Space Telescopes at the Space Telescope Science Institute, which is operated by the Association of Universities for Research in Astronomy, Inc., under NASA contract NAS 5-03127 for JWST. These observations are associated with program #2104. Based on observations made with the NASA/ESA Hubble Space Telescope, and obtained from the Hubble Legacy Archive, which is a collaboration between the Space Telescope Science Institute (STScI/NASA), the Space Telescope European Coordinating Facility (ST-ECF/ESAC/ESA) and the Canadian Astronomy Data Centre (CADC/NRC/CSA). This research is based on observations made with the NASA/ESA Hubble Space Telescope obtained from the Space Telescope Science Institute,

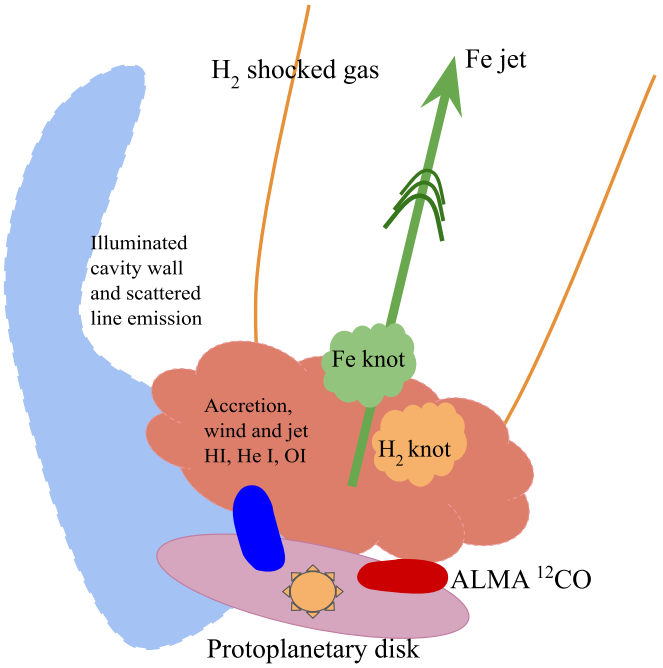

Figure 4. Cartoon of TMC1A's physical structure. The three major components that are traced by the hot gas lines are accretion onto the protostar, the jet, and the illuminated cavity wall. The disk and the cold wind as traced with ALMA are also indicated.

which is operated by the Association of Universities for Research in Astronomy, Inc., under NASA contract NAS 5-26555. This paper makes use of the following ALMA data: ADS/JAO. ALMA#2017.1.00212.S. ALMA is a partnership of ESO (representing its member states), NSF (USA), and NINS (Japan), together with NRC (Canada), MOST and ASIAA (Taiwan), and KASI (Republic of Korea), in cooperation with the Republic of Chile. The Joint ALMA Observatory is operated by ESO, AUI/NRAO, and NAOJ. The National Radio Astronomy Observatory is a facility of the National Science Foundation operated under cooperative agreement by Associated Universities, Inc.

We thank the anonymous referee for the helpful comments that have improved this letter. D.H. is supported by Center for Informatics and Computation in Astronomy (CICA) grant and grant No. 111J0353I9 from the Ministry of Education of Taiwan. D.H. also acknowledges support from the National Science and Technology Council of Taiwan through grant No. 111B3005191. H.C.'s research group is supported by an OPUS research grant (2021/41/B/ST9/03958) from the Narodowe Centrum Nauki. P.B. acknowledges the support of the Swedish Research Council (VR) through contract 2017-04924. The research of L.E.K. is supported by a research grant (19127) from VILLUM FONDEN. J.P.R. and Z.Y.L. are supported in part by NSF grant AST-1910106 and NASA grant 80NSSC20K0533. J.P.R. would like to further acknowledge the support of the Virginia Initiative on Cosmic Origins (VICO). The authors also acknowledge financial support by NASA through a grant from the STScI.

Facilities: JWST (NIRSPEC), ALMA, and HST (NICMOS).

Software: astropy (Astropy Collaboration et al. 2013, 2018), numpy (Harris et al. 2020), and matplotlib (Hunter 2007).

Appendix A
Centroid Alignment

We have used the HST and ALMA images taken a few years apart to characterize the physical structure around TMC1A. The dithered HST images were processed in 2005 April using MULTIDRIZZLE (v 3.1.0 Koekemoer). These data were directly downloaded from the MAST archive. The observations were taken in 1997 September. The long-baseline ALMA data are published in Bjerkeli et al. (2016), and were taken in 2017 October. Between when the HST, ALMA, and JWST data were taken, TMC1A has moved considerably.

To align the images, we have used the arc structure that is seen in the HST image and the JWST dust continuum image. Due to the positional uncertainty of HST/NICMOS, the images were aligned with a shift that corresponds to a proper motion of $(\mu_\alpha, \mu_\delta) = (0\farcs036\,\mathrm{yr}^{-1}, -0\farcs026\,\mathrm{yr}^{-1})$ to align the HST and JWST images (see Figure 5). The ALMA images are shifted by

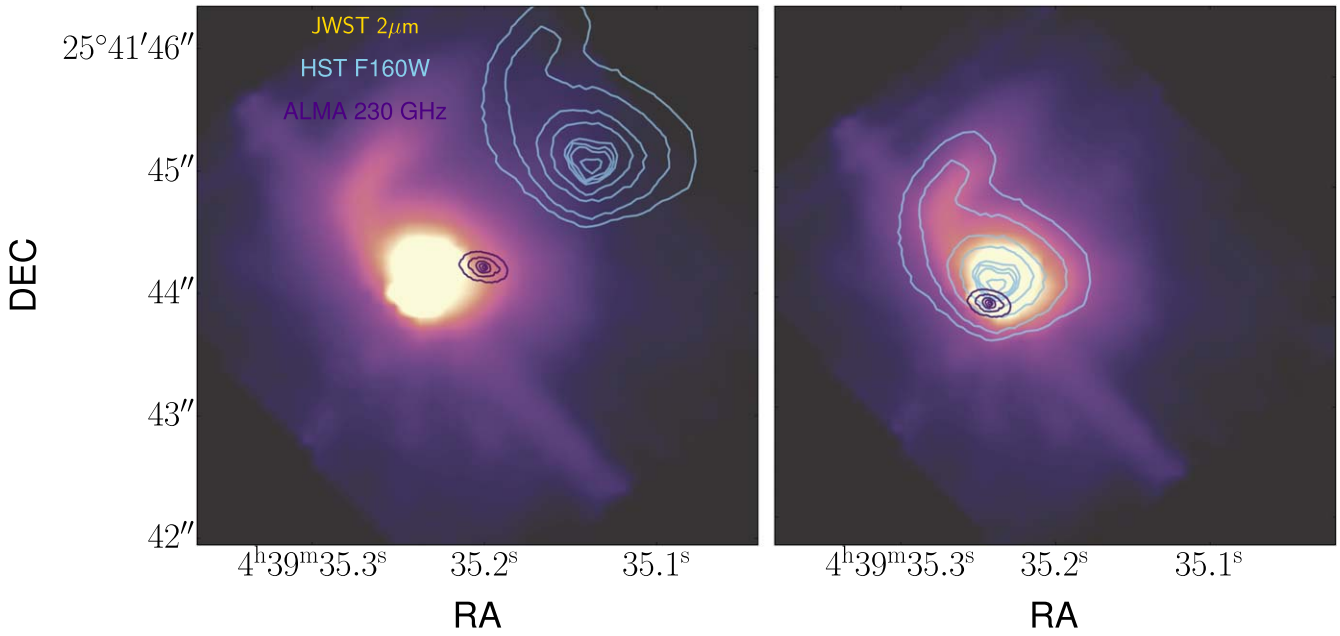

Figure 5. Left: original positions of the images. Right: aligned images after correcting for proper motion.

$\Delta\alpha = 0\farcs6$ and $\Delta\delta = -0\farcs26$ to align with the 2 μm image. We have used the long-baseline ALMA data from 2016, 2017, and 2022 to confirm that the misalignment between JWST and HST is due to the positional offsets. We note that the ALMA data are not perfectly centered on the 2 μm dust emission but are located a few pixels to the southeast.

Appendix B
VLT CRIRES versus JWST

Previous ground-based observations of rovibrational transitions of ^{12}CO of TMC1A show deep blueshifted absorption and redshifted emission (Herczeg et al. 2011). Figure 6 shows a comparison between the JWST H I Paβ and the averaged $v = 1 - 0$ line of ^{12}CO. Given the overlap in velocity space, the material that is responsible for the strong absorption in ^{12}CO may also be responsible for the deficit of emission in the blueshifted part of the H I lines.

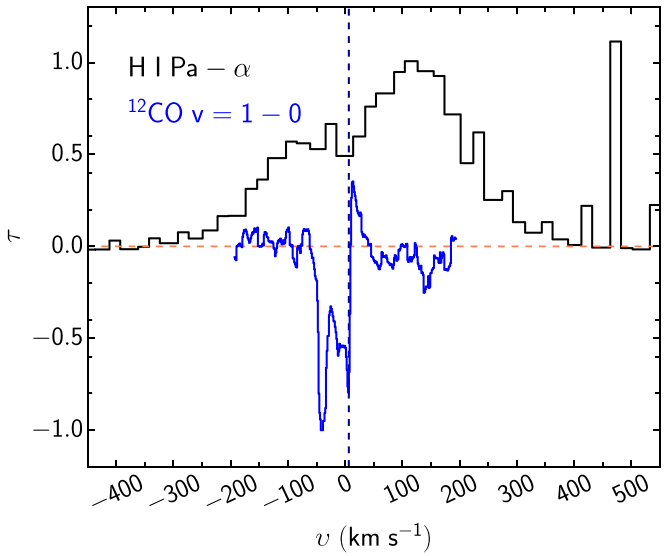

Figure 6. Comparison between ^{12}CO (4.65 μm) and H I (1.87 μm) normalized spectra.

ORCID iDs

D. Harsono https://orcid.org/0000-0001-6307-4195
P. Bjerkeli https://orcid.org/0000-0002-7993-4118
J. P. Ramsey https://orcid.org/0000-0002-3835-3990
K. M. Pontoppidan https://orcid.org/0000-0001-7552-1562
L. E. Kristensen https://orcid.org/0000-0003-1159-3721
J. K. Jørgensen https://orcid.org/0000-0001-9133-8047
H. Calcutt https://orcid.org/0000-0003-3393-294X
Z-Y. Li https://orcid.org/0000-0002-7402-6487
A. Plunkett https://orcid.org/0000-0002-9912-5705

References

Agra-Amboage, V., Cabrit, S., Dougados, C., et al. 2014, A&A, 564, A11
Allen, D. A., & Burton, M. G. 1993, Natur, 363, 54
Arce, H. G., Shepherd, D., Gueth, F., et al. 2007, in Protostars and Planets V, ed. B. Reipurth, D. Jewitt, & K. Keil (Tucson: Univ. of Arizona Press), 245
Astropy Collaboration, Price-Whelan, A. M., Sipőcz, B. M., et al. 2018, AJ, 156, 123
Astropy Collaboration, Robitaille, T. P., Tollerud, E. J., et al. 2013, A&A, 558, A33
Bally, J., & Lada, C. J. 1983, ApJ, 265, 824
Bjerkeli, P., van der Wiel, M. H. D., Harsono, D., Ramsey, J. P., & Jørgensen, J. K. 2016, Natur, 540, 406
Bushouse, H., Eisenhamer, J., Dencheva, N., et al. 2023, JWST Calibration Pipeline v1.9.6, Zenodo, doi:10.5281/zenodo.7714020
Davis, C. J., Stern, L., Ray, T. P., & Chrysostomou, A. 2002, A&A, 382, 1021
de A. Schutzer, A., Rivera-Ortiz, P. R., Lefloch, B., et al. 2022, A&A, 662, A104
de Valon, A., Dougados, C., Cabrit, S., et al. 2020, A&A, 634, L12
Di Francesco, J., Johnstone, D., Kirk, H., MacKenzie, T., & Ledwosinska, E. 2008, ApJS, 175, 277
Edwards, S., Fischer, W., Hillenbrand, L., & Kwan, J. 2006, ApJ, 646, 319
Edwards, S., Kwan, J., Fischer, W., et al. 2013, ApJ, 778, 148
Erkal, J., Manara, C. F., Schneider, P. C., et al. 2022, A&A, 666, A188
Evans, N. J. I., Dunham, M. M., Jørgensen, J. K., et al. 2009, ApJS, 181, 321
Frank, A., Ray, T. P., Cabrit, S., et al. 2014, in Protostars and Planets VI, ed. H. Beuther et al. (Tucson, AZ: Univ. Arizona Press), 451
Furlan, E., McClure, M., Calvet, N., et al. 2008, ApJS, 176, 184
Galli, P. A. B., Loinard, L., Bouy, H., et al. 2019, A&A, 630, A137
Green, J. D., Evans, N. J., II, Jørgensen, J. K., et al. 2013, ApJ, 770, 123
Greenfield, P., & Miller, T. 2016, A&C, 16, 41
Gusdorf, A., Anderl, S., Lefloch, B., et al. 2017, A&A, 602, A8
Harris, C. R., Millman, K. J., van der Walt, S. J., et al. 2020, Natur, 585, 357
Harsono, D., Bjerkeli, P., van der Wiel, M. H. D., et al. 2018, NatAs, 2, 646
Harsono, D., van der Wiel, M. H. D., Bjerkeli, P., et al. 2021, A&A, 646, A72
Hartigan, P., Morse, J. A., & Raymond, J. 1994, ApJ, 436, 125
Hartmann, L., & Kenyon, S. J. 1985, ApJ, 299, 462
Herbig, G. H. 1977, ApJ, 217, 693
Herczeg, G. J., Brown, J. M., van Dishoeck, E. F., & Pontoppidan, K. M. 2011, A&A, 533, A112
Hirano, N., Ho, P. P. T., Liu, S.-Y., et al. 2010, ApJ, 717, 58
Hull, C. L. H., Girart, J. M., Kristensen, L. E., et al. 2016, ApJL, 823, L27
Hunter, J. D. 2007, CSE, 9, 90
Jakobsen, P., Ferruit, P., Alves de Oliveira, C., et al. 2022, A&A, 661, A80
Karska, A., Herczeg, G. J., van Dishoeck, E. F., et al. 2013, A&A, 552, A141
Kramida, A. 2010, ADNDT, 96, 586
Kristensen, L. E., van Dishoeck, E. F., Benz, A. O., et al. 2013, A&A, 557, A23
Kristensen, L. E., van Dishoeck, E. F., Bergin, E. A., et al. 2012, A&A, 542, A8
Kurosawa, R., Harries, T. J., & Symington, N. H. 2006, MNRAS, 370, 580
Kwan, J., & Fischer, W. 2011, MNRAS, 411, 2383
Lahuis, F., van Dishoeck, E. F., Jørgensen, J. K., Blake, G. A., & Evans, N. J. 2010, A&A, 519, A3
Leung, C. M., & Brown, R. L. 1977, ApJL, 214, L73
Liang, L., Johnstone, D., Cabrit, S., & Kristensen, L. E. 2020, ApJ, 900, 15
May, P. W., Pineau des Forêts, G., Flower, D. R., et al. 2000, MNRAS, 318, 809
McCoey, C., Giannini, T., Flower, D. R., & Caratti o Garatti, A. 2004, MNRAS, 353, 813
Mundt, R., & Fried, J. W. 1983, ApJL, 274, L83
Muzerolle, J., Hartmann, L., & Calvet, N. 1998a, AJ, 116, 2965
Muzerolle, J., Hartmann, L., & Calvet, N. 1998b, AJ, 116, 455
Nisini, B., Antoniucci, S., & Giannini, T. 2004, A&A, 421, 187
Pascucci, I., Cabrit, S., Edwards, S., et al. 2022, arXiv:2203.10068
Persson, S. E., Geballe, T. R., McGregor, P. J., Edwards, S., & Lonsdale, C. J. 1984, ApJ, 286, 289
Plunkett, A. L., Arce, H. G., Mardones, D., et al. 2015, Natur, 527, 70
Podio, L., Codella, C., Gueth, F., et al. 2015, A&A, 581, A85
Pontoppidan, K. M., van Dishoeck, E. F., & Dartois, E. 2004, A&A, 426, 925
Pudritz, R. E., & Norman, C. A. 1983, ApJ, 274, 677
Rabenanahary, M., Cabrit, S., Meliani, Z., & Pineau des Forêts, G. 2020, A&A, 664, A118
Ray, T. P., & Ferreira, J. 2021, NewAR, 93, 101615
Shang, H., Krasnopolsky, R., Liu, C.-F., & Wang, L.-Y. 2020, ApJ, 905, 116
Shang, H., Li, Z. Y., & Hirano, N. 2007, in Protostars and Planets V, ed. B. Reipurth, D. Jewitt, & K. Keil (Tucson, AZ: Univ. Arizona Press), 261
Shu, F., Najita, J., Ostriker, E., et al. 1994, ApJ, 429, 781
Skrutskie, M. F., Cutri, R. M., Stiening, R., et al. 2006, AJ, 131, 1163
Snell, R. L., Dickman, R. L., & Huang, Y. L. 1990, ApJ, 352, 139
Snell, R. L., & Loren, R. B. 1977, ApJ, 211, 122
Tabone, B., Cabrit, S., Bianchi, E., et al. 2017, A&A, 607, L6
Tafalla, M., Santiago, J., Johnstone, D., & Bachiller, R. 2004, A&A, 423, L21
van Hoof, P. A. M. 2018, Galax, 6, 63
Yang, Y.-L., Evans, N. J., Karska, A., et al. 2022, ApJ, 925, 93
Yıldız, U. A., Kristensen, L. E., van Dishoeck, E. F., et al. 2015, A&A, 576, A109